Pulsed Inductive Plasma Acceleration: Performance Optimization Criteria

By: Kurt A. Polzin

Abstract

Optimization criteria for pulsed inductive plasma acceleration are developed using an acceleration model consisting of a set of coupled circuit equations describing the time-varying current in the thruster and a one-dimensional momentum equation. The model is nondimensionalized, resulting in the identification of several scaling parameters that are varied to optimize the performance of the thruster. The analysis reveals the benefits of underdamped current waveforms and leads to a performance optimization criterion that requires the matching of the natural period of the discharge and the acceleration timescale imposed by the inertia of the working gas. In addition, the performance increases when a greater fraction of the propellant is initially located nearer to the inductive acceleration coil. While the dimensionless model uses a constant temperature formulation in calculating performance, the scaling parameters that yield the optimum performance are shown to be relatively invariant if a self-consistent description of energy in the plasma is instead used.

Introduction

Pulsed inductive plasma accelerators are devices in which a capacitor is charged to an initial voltage and discharged through a coil to produce a high-current pulse. The field produced by this pulse ionizes propellant and inductively drives a current in the plasma formed near the face of the coil. Once the plasma is formed it can be accelerated and expelled at high exhaust velocity by the electromagnetic Lorentz body force arising from the interaction of the induced plasma current and the magnetic field produced by the current in the coil. Accelerator efficiency is defined as the ratio of jet kinetic power in the plasma to the total amount of electrical power supplied to the accelerator. Jahn [1] succinctly stated the following

inherent difficulties pertaining to both ionization and acceleration that must be overcome for an inductive plasma accelerator to operate efficiently:

> ". . . inductive discharges embody two inherent electrodynamic disadvantages to conversion efficiency which detract from their propulsive effectiveness. First, any delay in breakdown of the gas after application of the primary field pulse results in energy being dissipated in the external circuit, which, unlike that of the direct electrode devices, is complete without the gas loop. . . This difficulty might be relieved by providing a separate preionization mechanism or by operation at a sufficiently rapid repetition rate, but it is indicative of an inherent inefficiency in coupling of the external circuit to the plasma.
>
> ...
>
> Equally troublesome is the need to accomplish all the energy input to the gas before much motion of it has occurred. The current induced in the gas-loop 'secondary' depends on its mutual inductance with the external primary, and thus is a strong function of the physical separation of these two current paths. As they separate under the acceleration, the coupling rapidly becomes weaker."

While the governing physics makes the development of an efficient accelerator a difficult prospect, flat-coil planar-geometry inductive pulsed plasma thrusters, specifically the Pulsed Inductive Thruster (PIT) [2–4] illustrated schematically in Fig. 1, have several demonstrated and potential benefits that make this type of thruster worthy of continued investigation. The electrodeless nature mitigates the lifetime and contamination issues associated with electrode erosion inherent in conventional electric thrusters. Also, a wider variety of propellants are available for use when compatibility with metallic electrodes is no longer an issue. The PIT has demonstrated operation on propellants including ammonia (highest measured efficiency of ~50%), hydrazine, and CO_2, and there is no fundamental reason why they would not operate on other propellants such as H_2O. It is well known that pulsed accelerators can maintain constant specific impulse I_{sp} and efficiency over a wide range of input power levels by adjusting the pulse rate to maintain

a constant discharge energy per pulse. In addition, the PIT has demonstrated operation in a regime where efficiency is relatively constant over a wide range of I_{sp}. Finally, thrusters in this class can operate at high energy per pulse; as pulse rates increase with evolving in-space power capabilities, these inductive thrusters will be able to process very high levels of power to provide relatively high average thrust using a single thruster design.

In addition to flat-coil planar-geometry accelerators, one of the simplest and oldest pulsed inductive plasma acceleration devices in existence is the theta pinch [5,6]. Theta-pinch devices consist of a capacitor connected to a single- or multi-turn coil located external to the working gas. When the capacitor is discharged through the coil, current flows in the azimuthal (theta) direction and inductively breaks down the gas within the interior of the coil. A cylindrical current sheet forms as the current in the external coil inductively couples to the plasma by inducing azimuthal currents in the opposite direction. The induced current density interacts with the induced axial magnetic field to yield a radial Lorentz body force which compresses the plasma within the cylinder. A theta pinch accelerator is illustrated in Fig. 2 along with its derivative, the conical theta pinch, which blends the planar and theta-pinch geometries.

In addition to the current sheet compression process outlined in the previous paragraph, theta pinch devices with separate bias field coils have been used to produce plasma geometries known as compact toroids, where the magnetic field lines produced in the plasma close on themselves [7]. These plasma devices are typically classified by the relative strengths of the poloidal and toroidal magnetic fields, B_P and B_T, respectively. A compact toroid in which $B_P \approx B_T$ is known as a spheromak while that in which $B_P >> B_T$ is called a field-reversed configuration (FRC). Note that spheromaks possess both poloidal and toroidal plasma currents while the dominant currents in an FRC are only in the toroidal direction. A cursory examination of the fusion literature reveals that FRC plasmas are relatively dense and coherent structures that can be accelerated by an externally-applied magnetic field, making them potentially interesting for space propulsion. The translation and acceleration of FRC plasmas has been achieved

using a linear series of theta pinches [8] and magnetic mirrors [9]. They have been shown to be quite stable, maintaining their cohesion even at super-Alfvénic speeds. Since the FRC plasma structure excludes external magnetic fields, it doesn't encounter the potential issues associated with plasma detachment from magnetic field lines inherent in magnetic nozzle-based propulsion concepts. Several research-level thrusters have been developed to explore the usefulness of low-temperature FRC plasma (plasmoid) propulsion [10–12].

In this article, we describe a model for pulsed inductive plasma acceleration that consists of a set of electrical circuit equations coupled to a one-dimensional momentum equation. Although it does not incorporate the detailed physics of 2D and 3D magnetohydrodynamic models [13,14] the one-dimensional model has shown good qualitative and quantitative agreement with experimental performance data for inductive thrusters [2]. The model consists of a set of coupled, first-order ordinary differential equations that can be nondimensionalized to identify a set of parameters that control the scaling of accelerator performance [15]. The model will be described in general and then specialized for the flat-coil planar-geometry to develop solutions which further elucidate the effect various parameters have on performance. While used here for the flat-coil geometry, the model has been used in modeling FRC plasmas [16] and translating theta-pinch-like geometries commonly associated with coilguns [17,18], which are the inductive equivalent of railguns. In each case the general insights developed for the flat-coil geometry have been shown to hold true for these other types of accelerators.

Governing Equations

A. Electrical Circuit Model

A lumped-element circuit model for a pulsed inductive accelerator is presented in Fig. 3a and redrawn in Fig. 3b so as to permit the application of Kirchoff's law to the two current loops. The external circuit (left side of the figure) possesses capacitance C, external inductance L_0, resistance R_e, and acceleration coil

inductance L_C. The plasma has an inductance equal to L_p and a bulk plasma resistance R_p. The two circuits are inductively coupled through the acceleration coil, which acts as a transformer possessing mutual inductance M. The value of M is a function of the current sheet position z. The time-varying behavior of this circuit is governed by the following coupled set of first-order ordinary differential equations:

$$\frac{dI_1}{dt} = \frac{VL_p + (MI_1 + I_2L_p)(dM/dt) - I_2MR_p - I_1R_eL_p}{L_p(L_0 + L_C) - M^2} \tag{1a}$$

$$\frac{dI_2}{dt} = \frac{M(dI_1/dt) + I_1(dM/dt) - I_2R_p}{L_p} \tag{1b}$$

$$\frac{dV}{dt} = -\frac{I_1}{C} \tag{1c}$$

where V is the voltage on the capacitor, initially at a value of V_0. In the planar-geometry configuration where the conductors of the coil complete a single turn, the geometric configuration of the plasma and coil currents are sufficiently similar to approximate $L_C \approx L_p$, which will be assumed for the remainder of this document.

If there exists no simple formula for the mutual inductance between the coil and plasma, then the inductance can be calculated using finite element methods. However, for the planar-geometry configuration where $L_C \approx L_p$, an empirically-developed equation for the mutual inductance has proven to be a relatively accurate substitute for an exact solution. Following Lovberg and Dailey [17], the total inductance of the system can be written as

$$L_{tot}(z) = L_0 + L_p(z) \tag{2}$$

where L_p is the position-varying inductance (called hereafter the plasma inductance), which is equal to the total inductance presented to the circuit by the circuit elements on the right side of the dashed line in Fig. 3b. Based on experimental measurements, it has been found that the plasma inductance as a function of axial current sheet position can be modeled as

$$L_p(z) = L_C\left[1 - \exp\left(-\frac{z}{z_0}\right)\right] \tag{3}$$

where z_0 is defined as the electromagnetic decoupling length. Another way to think of L_p is as a Thévenin equivalent inductance for all the elements to the right of the dashed line in Fig. 3b.

Neglecting the resistances in the circuit, the series and parallel inductances in the system can be approximately combined into one inductive element with the value

$$L_{tot} = L_0 + \left(L_C - \frac{M^2}{L_C}\right) \tag{4}$$

By equating the terms in the parentheses with the plasma inductance L_p from Eq. 3, we find that the mutual inductance is given as

$$M = L_C \exp\left(-\frac{z}{2z_0}\right) \tag{5}$$

The preceding equation can be differentiated to yield

$$\frac{dM}{dt} = -\frac{L_C}{2z_0}\exp\left(-\frac{z}{2z_0}\right)\frac{dz}{dt} \tag{6}$$

which governs the time-varying behavior of the mutual inductance and completes the set of electrical circuit equations.

B. Acceleration Model

In the idealized "snowplow" model, the plasma sheet consists of a current sheet that moves forward, entraining and accelerating any gas that it encounters. The propellant mass in the current sheet as a function of time can be written as

$$m(t) = m_0 + \int_{t=0}^{t} \rho_A v_z dt \tag{7}$$

where $\rho_A = \rho_A\big(z(t)\big)$ is the linear mass density distribution and v_z is the sheet velocity. The term m_0 represents the initial mass of propellant in the sheet while the integral term represents the mass accumulated by the sheet as it moves away from the acceleration coil. (Note that while the ideal snowplow model is often employed in pulsed plasma modeling, the current sheet in a real accelerator only entrains a fraction of the total available propellant, depending largely upon the plasma properties.)

The momentum equation for the current sheet is a statement of Lenz's law and can be written as

$$-I_1 I_2 \frac{\partial M}{\partial z} = \rho_A v_z^2 + m(t) \frac{dv_z}{dt} \tag{8}$$

with the negative sign arising due to the assumed positive directions of currents I_1 and I_2. The left-hand side represents the self-field electromagnetic force while the first term on the right-hand side represents the momentum investment associated with entraining propellant that the current sheet encounters while the second term involves further acceleration of the already entrained propellant. It has been shown from

magnetic field energy considerations that the self-field electromagnetic force term can equivalently be written as [17]

$$\frac{I_1^2}{2}\frac{\partial L_p}{\partial z} = \frac{L_C I_1^2}{2z_0}\exp\left(-\frac{z}{z_0}\right) \tag{9}$$

where L_p for the planar-geometry coil is given in Eq. 3.

C. Plasma Model

While the model of the plasma properties can generally be complex, simpler plasma models can be employed. The simplest is to assume a Spitzer resistivity [17],

$$\eta = 6 \times 10^{-4} T_e^{-3/2} \tag{10}$$

with the electron temperature T_e (in units of eV) treated as a free parameter. A description of the plasma energy within the framework of the one-dimensional model has been developed [19], but it involves additional calculations and the tracking of various plasma state properties. While the added complexity does provide the capability to conserve energy within the system and perform calculations for different gases without an *a priori* assumption of plasma temperature, the scaling terms identified using the simpler model are relatively invariant in terms of the effects on thruster optimization.

To complete the model, the plasma resistivity η is used to estimate the current sheet width and plasma resistance. The growth in the current sheet width δ_a can be estimated by assuming the process occurs through resistive diffusion of the magnetic field, resulting in

$$\delta_a = \sqrt{\delta_s^2 + \frac{\eta}{\mu_0} t} \tag{11}$$

where δ_s is an estimate of the initial current sheet thickness [$\delta_s = \delta_a$ (t = 0)]. Modeling the current sheet as a homogeneous ring of plasma, with inner and outer radii of *a* and *b*, respectively, the total plasma resistance is approximated as

$$R_p \approx \frac{\pi\eta(b+a)}{\delta_a(b-a)}. \tag{12}$$

D. Model Nondimensionalization

The following dimensionless terms are selected to aid in the conversion of the dimensional equations to a nondimensionalized set:

$$I_1^* = \frac{1}{V_0}\sqrt{\frac{L_0}{C}} I_1 \tag{13a}$$

$$I_2^* = \frac{1}{V_0}\sqrt{\frac{L_0}{C}} I_2 \tag{13b}$$

$$t^* = \frac{t}{\sqrt{L_0 C}} \tag{13c}$$

Starting from this basis, in the course of nondimensionalizing the governing equations the following additional nondimensional variables naturally appear in the equation set:

$$z^* = \frac{z}{z_0} \tag{14a}$$

$$M^* = \frac{M}{L_C} \tag{14b}$$

$$V^* = \frac{V}{V_0} \tag{14c}$$

$$v_z^* = \frac{\sqrt{L_0 C}}{z_0} v_z \tag{14d}$$

If the propellant distribution is some function of axial position ($\rho_A = \rho_0 f(z)$) and the total amount of propellant mass per pulse is m_{bit}, then the mass accumulation equation can be nondimensionalized as

$$m^* = m_0^* + \int_0^{t^*} \rho^* f(z^*) v_z^* dt^* \tag{15}$$

where $m_0^* = m_0/m_{\text{bit}}$ and $\rho^* = \rho_0 z_0/m_{\text{bit}}$.

Collecting the entire set of first order ordinary differential equations and writing them in dimensionless form yields

$$\frac{dI_1^*}{dt^*} = [L^* V^* + (M^* I_1^* + I_2^*)(dM^*/dt^*) - I_2^* M^* L^* \psi_2 - I_1^* L^* \psi_1]/[(L^* + 1) - (M^*)^2] \tag{16a}$$

$$\frac{dI_2^*}{dt^*} = M^* \frac{dI_1^*}{dt^*} + I_1^* \frac{dM^*}{dt^*} - I_2^* L^* \psi_2 \tag{16b}$$

$$\frac{dV^*}{dt^*} = -I_1^* \tag{16c}$$

$$\frac{dM^*}{dt^*} = -\frac{1}{2} \exp\left(-\frac{z^*}{2}\right) v_z^* \tag{16d}$$

$$\frac{dz^*}{dt^*} = v_z^* \tag{16e}$$

$$\frac{dv_z^*}{dt^*} = [\alpha (I_1^*)^2 \exp(-z^*) - \rho^* f(z^*)(v_z^*)^2]/m^* \tag{16f}$$

$$\frac{dm^*}{dt^*} = \rho^* f(z^*) v_z^* \tag{16g}$$

The initial conditions for the set of nondimensional differential equations are

$$I_1^*(0) = 0 \tag{17a}$$

$$I_2^*(0) = 0 \tag{17b}$$

$$V^*(0) = 1 \tag{17c}$$

$$M^*(0) = 1 \tag{17d}$$

$$z^*(0) = 0 \tag{17e}$$

$$v_z^*(0) = 0 \tag{17f}$$

$$m^*(0) = m_0/m_{\text{bit}} \tag{17g}$$

Note that $\rho^* = 0$ when the propellant is loaded like a slug ($m_0 = m_{\text{bit}}$).

Scaling Parameters

During the course of nondimensionalization, several new terms appear in (16). These new terms are the relevant scaling parameters of the system of equations and are defined as

$$L^* = \frac{L_0}{L_C} \tag{18a}$$

$$\psi_1 = R_e\sqrt{\frac{C}{L_0}} \tag{18b}$$

$$\psi_2 = R_p\sqrt{\frac{C}{L_0}} \tag{18c}$$

$$\alpha = \frac{C^2V_0^2L_C}{2m_{\text{bit}}z_0^2} \tag{18d}$$

We proceed in this section with a brief discussion of the meanings of the scaling parameters.

A. Inductance Ratio: L^*

During a current pulse, the moving plasma increases the circuit's inductance from L_0 to a maximum possible value of $L_0 + L_C$ (i.e., L_C is equal to the maximum inductive 'stroke' ΔL). The fractional change

of inductance, $(L^*)^{-1} = \Delta L/L_0$, in a pulsed electromagnetic accelerator provides a measure of efficiency [20], as this ratio is indicative of the fraction of energy that can be deposited into electromagnetic acceleration of the gas. In an efficient pulsed inductive accelerator, the value of L^* must be much less than unity or $L_C \gg L_0$.

B. Critical Resistance Ratios: ψ_1 and ψ_2

The ratios ψ_1 and ψ_2 appear in the circuit equations and control the nature of the current waveforms. To elucidate the physical meanings of these ratios, we attempt to find limiting solutions to (16a)–(16c). Decoupling the current sheet dynamics (i.e., the acceleration and sheet motion) from the problem allows us to set $M^* = 1$ for all time, dramatically simplifying the circuit equations. Under this assumption, the circuit equations can be rewritten as

$$\frac{d^2 I_1^*}{dt^{*2}} + (\psi_1 + \psi_2)\frac{dI_1^*}{dt^*} + I_1^* = \psi_2^2 L^* I_2^* \tag{19a}$$

$$\frac{dI_1^*}{dt^*} - \frac{dI_2^*}{dt^*} = \psi_2 L^* I_2^* \tag{19b}$$

If the right-hand side of the first equation is small (≈ 0), then the solution for I_1^* is

$$I_1^* = A_0 \exp(-\Psi t^*) \sin\left[(1-\Psi^2)^{1/2} t^*\right] \tag{20}$$

where we have introduced the new dimensionless parameter $\Psi \equiv (\psi_1 + \psi_2)/2$. The solution is underdamped (ringing) for $\Psi < 1$, critically damped for $\Psi = 1$, and overdamped for $\Psi > 1$. If the right-hand side in Eq. 19b is also small, then the induced current in the plasma mirrors the current in the coil

$$I_2^* = I_1^* . \tag{21}$$

The fact that the current waveform depends on the sum of ψ_1 and ψ_2 implies that within a portion of the (ψ_1,ψ_2) parameter space, contours of constant performance should generally follow the contours given by

$$(\psi_1 + \psi_2)/2 = \text{constant.} \tag{22}$$

To neglect the nonlinearities present in the circuit equations and arrive at the limiting solutions given above, the values of L^* and ψ_2 must be such that

$$\psi_2^2 L^* \ll 1 \tag{23a}$$

$$\psi_2 L^* \ll 1 \tag{23b}$$

Therefore, we expect a feature or transition in a contour plot of accelerator performance as either $\psi_2^2 L^*$ or $\psi_2 L^*$ approaches unity.

C. Dynamic Impedance Parameter: α

The dynamic impedance parameter α can be recast as the product of several important ratios

$$\alpha = \frac{C^2 V_0^2 L_C}{2 m_{\text{bit}} z_0^2} = \frac{1}{8\pi^2} \frac{C V_0^2/2}{m_{\text{bit}} v_z^2/2} L^* \left(\frac{2\pi\sqrt{L_0 C}}{L_0/\dot{L}} \right)^2 \tag{24}$$

where $\dot{L}$ is the dynamic impedance, defined as $v_z L'$, and L' is the effective inductance per unit length, equal to L_C/z_0. The ratio of the initial stored energy ($CV_0^2/2$) to the plasma kinetic energy ($m_{\text{bit}} v_z^2/2$) is recognized as the inverse of thrust efficiency and will always be greater than one. The term L^* was discussed in a previous section. The final term is the ratio of the natural period of the driving external

circuit $2\pi\sqrt{L_0 C}$ to the time interval $L_0/\dot{L}$, over which the motion of the plasma increases the inductance of the circuit by one unit of L_0. The former is the timescale on which the external circuit naturally operates, while the latter is the timescale on which the current sheet remains electromagnetically coupled to the acceleration coil. For a given configuration, there exists an optimum value of α where the electromagnetic coupling timescale is matched to the frequency of the external circuit, allowing for optimum transfer of stored electrical energy into directed kinetic energy.

Generating Solutions

The set of coupled first-order ordinary differential equations (ODEs) given in (16) can be solved numerically once the mass distribution and the set of scaling parameters given in (18) are specified. The performance metric chosen for this study is the thrust efficiency, which is written in terms of nondimensional parameters as

$$\eta = \frac{m^*(v_z^*)^2}{2L^*\alpha} \tag{25}$$

where $m^*$and v_z^* are evaluated at the end of the calculation. Optimization of performance in pulsed inductive plasma accelerators is concerned with adjusting the scaling parameters to increase the thrust efficiency of the device.

The computation is advanced in time through the first half-cycle of the discharge until the coil current crosses zero. It is well known in pulsed plasma accelerator research that when the accelerator current passes through zero, it is passing through a local maximum in $|dI_1^*/dt^*|$. During this coil current reversal, the high current rise rate can cause a new current sheet to form at the face of the coil, especially if the current sheet imperfectly sweeps the propellant during the first half-cycle leaving residual gas behind. This new current sheet is known as a “crowbar discharge,” and it effectively short-circuits the initial

current sheet so no additional energy can be added. We discontinue the calculation at this reversal point because the plasma physics involved in the crowbar discharge process is not contained in the model.

The crowbar discharge phenomenon causes difficulties in the calculation of η in cases where the current sheet has not advanced far enough during the first half-cycle to have encountered all the gas. In these instances, the computed mass in the current sheet after the first half-cycle will be smaller than m_{bit} (i.e., $m^* < 1$). However, from a performance perspective, m_{bit} was injected into the system, so $m^* = 1$ is the proper value to use in Eq. (25). We must therefore apply a correction to the final velocity to account for the mass that is unswept after the first half-cycle. This can be accomplished using conservation of momentum such that

$$(v_z^*)_{\mathrm{corr}} = (v_z^*)|_f \; m^*|_f \tag{26}$$

where $(v_z^*)_{\mathrm{corr}}$ is the 'corrected' velocity and the velocity and mass in the sheet are evaluated for the 'final' timestep f as determined by the conditions above. As a consequence, the velocity of the current sheet is reduced as it entrains the remaining gas it encounters after the end of the first half-cycle.

The slug mass loading ($\rho^* = 0, m^*(0) = 1$), while not physically realizable in a gas-fed system, allows for the exploration of the parameter space while minimizing the effects of the mass distribution on the acceleration scheme. The function $\rho^* f(z^*)$ can be arbitrarily chosen to evaluate the effect other gas distributions have on performance. Data show that a triangular mass distribution of the form

$$\rho^* f(z^*) = \begin{cases} \frac{\rho_0 z_0}{m_{bit}}[1 - (z^*/\delta_m^*)], & z^* \le \delta_m^* \\ 0, & z^* > \delta_m^* \end{cases} \tag{27}$$

is a good quantitative match to the distribution found in the PIT MkV and MkVa [2]. The value of ρ_0 is calculated such that for a distribution as specified in (27) with a nondimensional mass depth δ_m^* the value of m^* when all gas is entrained is unity.

For computed performance presented in subsequent sections, unless they are being varied, the values of the nondimensional parameters are $L^* = 0.121$, $\psi_1 = 0.05$, $\psi_2, = 0.13$, $\alpha = 2.1$, and $\delta_m^* = 0.53$. These values roughly correspond to the parameters of the PIT MkVa accelerator [2], which to date represents the iteration of the PIT with the highest demonstrated efficiency (on ammonia propellant).

Results and Optimization

The system of nondimensional equations was solved by varying the values of different scaling parameters to learn the effect each had on accelerator performance. These results led to several insights regarding performance optimization in these accelerators.

A. Propellant Distribution

Contours of constant thrust efficiency as a function of α and ψ_1 are presented for the triangular mass distribution in Fig. 4a and for the slug mass distribution in Fig. 4b. We observe that propellant loading has a large influence on thrust efficiency, reducing from a maximum of approximately 70% for a slug mass to roughly 50% for a triangular mass loading. The loss in efficiency can be understood as follows. An inductively driven current sheet propagating with substantial velocity into propellant experiences significant drag (drag force $\propto (v_z^*)^2$) as it entrains propellant. At the same time the electromagnetic driving force applied to the current sheet by the coil decreases exponentially with increasing axial position. As a consequence, the thrust efficiency can be high for a slug mass loading, but for less slug-like propellant loadings the efficiency drops precipitously due to large mass entrainment losses incurred after the current sheet has appreciable velocity.

B. Resistance Ratios

It was found through numerical solutions that a change in either ψ_1 and ψ_2 will affect the performance of the circuit, with more underdamped circuits yielding higher performance. The fact that either ratio has this effect was predicted in the discussion of limiting solutions to the circuit equations through the introduction of the parameter Ψ, which combined ψ_1 and ψ_2. The effect the critical resistance ratios have on performance is understood as follows. In a pulsed inductive accelerator we find that, neglecting mass entrainment losses, the total impulse imparted to the propellant scales as

$$\text{Impulse} \sim \int (I_1^*)^2 \exp[-z^*(t^*)] dt^* \tag{28}$$

This means the force accelerating the plasma drops exponentially as the sheet moves away from $z^* = 0$, even if the peak current could somehow be maintained. Therefore, to perform maximum work and achieve efficient pulsed inductive acceleration the highest possible peak current must be reached before the sheet moves far from the back-end of the accelerator (i.e., near $z^* = 0$), which occurs in the case of underdamped pulse circuits. Any attempt to lower the peak current and extend the current pulse length will result in a less efficient acceleration process with a higher fraction of the total energy in the circuit dissipated instead of performing useful work on the plasma.

C. Dynamic Impedance Optimization

Returning to Fig. 4a, we observe that as expected the efficiency possesses a local maximum with respect to α, and that this maximum occurs in the neighborhood of α between 1 and 3. The resulting calculations show an increasing plasma exit velocity as α is increased. This implies a decrease in time that the current sheet is electromagnetically coupled to the current in the coil. These observations are consistent with our interpretation of α as a dynamic impedance matching parameter.

To further demonstrate the usefulness of the dynamic impedance parameter in predicting the optimum in performance, we compare simulation results with experimental data obtained for the PIT MkVa and MkV. The capacitance for the MkV was half that of the MkVa, resulting in critical resistance ratios of $\psi_1 = 0.035$ and $\psi_2 = 0.09$. Simulation results showing the efficiency as a function of α for both thrusters are presented in Fig. 5. Experimental performance measurements are also given on the same graph for each thruster operating on ammonia propellant. The experimental data compare quite favorably, both qualitatively and quantitatively, with the computed performance. The lower capacitance places the MkV experimental data all to the left side of the local maximum in efficiency, while the MkVa data span the local maximum in efficiency where the impedance match between the electrical circuit and the plasma load is optimized. The agreement with experimental data is interesting since the dimensionless performance model cannot differentiate between various propellant species on the basis of internal and radiative energy sinks because it lacks an equation for the conservation of energy and models for plasma state properties.

Additional Insights

The simplified 1-D model used as the basis of analysis in this paper is attractive because it permits the identification of performance trends as a function of controllable parameters without requiring complex and computationally intensive two- and three-dimensional magnetohydrodynamic simulations [13,14]. However, this acceleration model is limited because it lacks a time-accurate description of the energy in the plasma, relying instead on an assumed, constant plasma temperature. While this does permit a coarse estimate of a constant plasma resistivity, the temperature and plasma properties are essentially decoupled from the system and cannot provide a self-consistent accounting of the time-varying transfer of energy from the external circuit into the plasma.

A recent article investigated the issue of energy conservation within the framework of the 1-D acceleration model [19]. Specifically, a model with an assumed constant temperature that is independently chosen *a priori* does not allow for a fully-accurate representation of the time-varying energy distribution in the plasma. Incorporating real gas properties and an energy equation into the model permits the more accurate determination of the plasma temperature for each time step of the solution. While a full discussion of the detailed modeling is beyond the scope of the present publication, the salient features of the improved model can be summarized as follows.

To improve upon the constant plasma temperature approximation, the pulsed inductive acceleration model governing equations were revised and enhanced to include a statement that permitted the calculation of the energy in the plasma, subsequently allowing for calculation of the evolving plasma pressure and temperature consistent with the time-varying energy flux into the plasma. The plasma temperature is obtained using a non-ideal, real-gas equation of state relationship to close the system. Once the plasma pressure, density, and temperature are known, other plasma state properties that affect the thruster performance calculation, such as ionization fraction, specific heat ratio, and plasma resistivity, can be found at every time step during the course of generating the solution. It is the inclusion of a real-gas equation of state and the calculation of the state properties that allow tailoring of the model for different propellants, which had not been previously possible within the 1-D modeling framework. Furthermore, the partitioning of energy in the accelerator is calculated as part of the solution process, tracking the evolution of energy in different readily-identifiable modes.

Computed efficiencies in the MkV configuration as a function of α for both the free-parameter (simplified) model of the present work and the self-consistent energy-equation model (for argon propellant) are presented in Fig. 6. In this figure the temperatures selected for use in the simplified model are over a range from 3–9 eV as indicated for their respective curves on the graph. All other things being equal, as α is increased the mass bit is reduced. In the previous sections where the simplified 1-D model

without an energy equation was used, it was found that the plasma kinetic energy was maximized at a given value of α. Within the constant T_e formulation, at lower mass bits the non-conserved thermal energy in the plasma is much smaller and less important relative to the other energy sinks (namely plasma kinetic energy and magnetic field energy). When using the energy equation formulation, as α is increased (from the left side of the optimum in efficiency), the thruster more readily deposits energy into directed plasma kinetic energy yielding more efficient acceleration and a commensurate reduction of the plasma heating sink. In both cases, the efficiency is increasingly less sensitive to the value of T_e as the optimum α is approached and exceeded, whether temperature is selected as a free parameter and fixed for the duration of the simulation or calculated self-consistently within the model containing the energy equation.

Conclusion

The nondimensionalization of a model for pulsed inductive plasma acceleration resulted in the identification of a set of parameters that control the scaling of performance in these devices. The physical meanings of the scaling parameters and their effects on accelerator performance can be explored through theoretical arguments and numerical solutions of the governing equations. The following insights can be gained with respect to performance optimization in pulsed inductive plasma accelerators.

- There exists a value of the dynamic impedance parameter α for which thrust efficiency is maximized. This optimum corresponds to a matching of the driving circuit's natural oscillation time scale to the residence time scale of the current sheet in the acceleration zone.

- Efficiency and exhaust velocity increase when the critical resistance ratios ψ_1 and ψ_2 (or equivalently Ψ) decrease in value. This is because the current must peak while the sheet is still close to the back end of the accelerator (i.e., near $z^* = 0$) is to impart maximum impulse to the plasma. Consequently, the greater initial currents found in underdamped circuits (relative to

critically damped circuits operating at the same discharge energy) are preferable for higher performance.

- Performance increases as a greater fraction of the propellant is loaded close to the back-end of the accelerator, with efficiency maximized for a slug mass loading. This is primarily due to the drag losses associated with a moving current sheet entraining and accelerating any propellant it encounters.

- Efficiency increases for decreasing values of the inductance ratio (L^*) as this represents an increase in the fraction of energy that can be deposited into electromagnetic acceleration of the propellant.

- The optimum efficiency, and the value of α where this optimum occurs, is relatively invariant whether predicted using the model employing a constant temperature plasma description or using a self-consistent energy equation formulation because at the optimum efficiency the thermal energy sink is small relative to the plasma kinetic energy.

The general model for pulsed inductive plasma acceleration was tailored to a planar-geometry coil configuration primarily because the most thoroughly-developed pulsed inductive thruster is of this type. However, the insights developed regarding the physical meanings of the scaling parameters and identification of relevant trends in efficiency data are broadly useful in that they are applicable to the entire class of pulsed inductive plasma accelerators.

Acknowledgements

The author is grateful to Michael LaPointe, who carefully reviewed the manuscript and suggested many corrections and changes that greatly improved the quality of the manuscript, and to Anita Beatty for helping to assemble this document. This work was made possible through continued NASA Marshall Space Flight Center management support from Jim Martin.

References

[1] Jahn, R.G. *Physics of Electric Propulsion*; McGraw-Hill: New York, 1968.

[2] Dailey, C.L.; Lovberg, R.H. The PIT MkV Pulsed Inductive Thruster. NASA-CR-191155; National Aeronautics and Space Administration, July **1993**.

[3] Lovberg, R.H.; Dailey, C.L. Large Inductive Thruster Performance Measurement. AIAA J., **1982**, *20* (7), 971-977.

[4] Polzin, K.A. Comprehensive Review of Planar Pulsed Inductive Plasma Thruster Research and Technology. J. Propuls. Power, May-Jun **2011**, *27* (3), 513-531.

[5] Lovberg, R.H. Investigation of Current-sheet Microstructure. AIAA J., Jul **1966**, *4* (7), 1215-1222.

[6] Alidières, M.; Aymar, R.; Koechlin, F.; Jourdan, P.; Samain, A. Shock and Current Sheet Structure in a Theta-pinch Configuration. Phys. Fluids, Jun **1970**, *13* (6), 1525-1532.

[7] Tuszewski, M. Field Reversed Configurations. Nuclear Fusion, Nov **1988**, *28* (11), 2033-2092.

[8] Hoffman, A.L.; Gurevich, P.; Grossnickle, J.; Slough, J.T. Inductive Field-reversed Configuration Accelerator for Tokamak Fueling. Fusion Sci. Technol., Sept **1999**, *36* (2), 109-125.

[9] Rej, D.J.; Armstrong, W.T.; Chrien, R.E.; Klingner, P.L.; Linford, R.K.; McKenna, K.F.; Sherwood, E.G.; Siemon, R.E.; Tuszewski, M.; Milroy, R.D. Experimental Studies of Field-reversed Configuration Translation. Phys. Fluids, Mar **1986**, *29* (3), 852-862.

[10] Eskridge, R.H.; Fimognari, P.J.; Martin, A.K.; Lee, M.H. Design and Construction of the PT-1 Prototype Plasmoid Thruster. AIP Conference Proceedings 2006, 813 (1), 474-483.

[11] Kirtley, D.; Gallimore, A.D.; Haas, J.; Reilly, M. High Density Magnetized Toroid Formation and Translation within XOCOT: An Annular Field Reversed Configuration Plasma Concept. IEPC-2007-41, 30th International Electric Propulsion Conference, Florence, Italy, Sept 2007.

[12] Slough, J.; Kirtley, D.; Weber, T. Preliminary Performance Measurements of the Air-Breathing ELF Thruster. Joint Army, Navy, NASA, Air Force (JANNAF) Propulsion Meeting, Orlando, FL, 2008.

[13] Mikellides, P.G.; Ratnayake, N. Modeling of the Pulsed Inductive Thruster Operating with Ammonia Propellant. J. Propuls. Power **2007**, *23* (4), 854-862.

[14] Mikellides, P.G.; Villarreal, J.K. High energy pulsed inductive thruster modeling operating with ammonia propellant. J. Appl. Phys. **2007**, *102*, 103301.

[15] Polzin, K.A.; Choueiri, E.Y. Performance Optimization Criteria for Pulsed Inductive Plasma Acceleration. IEEE Trans. Plasma Sci. **2006**, *34* (3), 945-953.

[16] Martin, A.K.; Eskridge, R.H. Electrical Coupling Efficiency of Inductive Plasma Accelerators. J. Phys. D: Appl. Phys. **2005**, *38* (23), 4168-4179.

[17] Kim, S.-W.; Jung, H.-K.; Hahn, S.-Y. Optimal Design of Multistage Coilgun. IEEE Trans. Magnetics **1996**, *32* (2), 505-508.

[18] Polzin, K.A.; Adwar, J.E.; Hallock, A.K. Optimization of Electrodynamic Energy Transfer in Coilguns with Multiple, Uncoupled Stages. IEEE Trans. Magnetics **2013**, *49* (4), 1453-1460.

[19] Polzin, K.A.; Sankaran, K.; Ritchie, A.G.; Reneau, J.P. Inductive Pulsed Plasma Thruster Model with Time-Evolution of Energy and State Properties. J. Phys. D: Appl. Phys. **2013**, *46*, 475201.

[20] Lovberg, R.H.; Hayworth, B.R.; and Gooding, T. The use of a coaxial plasma gun for plasma propulsion. Tech. Rep. AE62-0678, May **1962**, G.D. Convair.

Bibliography

N/A

Table Captions

N/A

Figure Captions

Figure 1: Schematic showing the basic operation of a planar pulsed inductive plasma accelerator. After Ref. [3]. Portions of the original reprinted with permission from R.H. Lovberg.

Figure 2: Schematic showing (a) a theta pinch and (b) a conical theta pinch pulsed inductive accelerator. After Ref. [1]. Portions of the original reprinted with permission from R.G. Jahn.

Figure 3: (a) General lumped-element circuit model and (b) equivalent circuit model of a pulsed inductive accelerator.

Figure 4: Contour plots of inductive accelerator efficiency as a function of α and ψ_1 for (a) a triangular mass distribution and (b) a slug mass distribution. The fixed nondimensional parameters in these computations are $\psi_2 = 0.13$ and $L^* = 0.121$. From Ref. [15].

Figure 5: Comparison between computed accelerator efficiencies as a function of α and PIT MkV and MkVa performance data. Data is from [2]. Figure reproduced from Ref. [4].

Figure 6: Simulated efficiencies for the PIT MkV calculated using the one-dimensional model where the temperature was selected as a fixed parameter and the model of Ref. [19] containing the energy-conservation formulation. From Ref. [19].

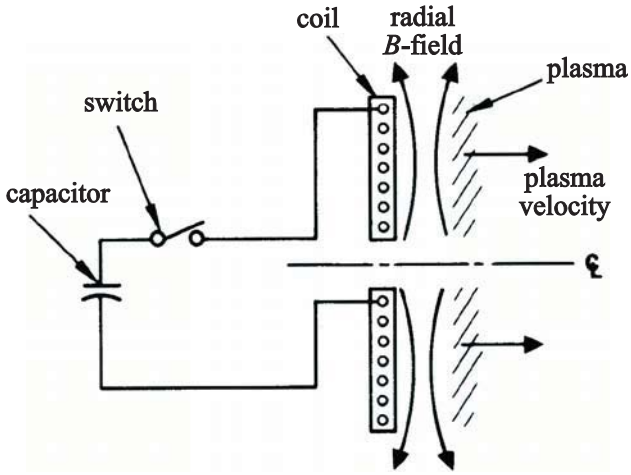

Figure 1

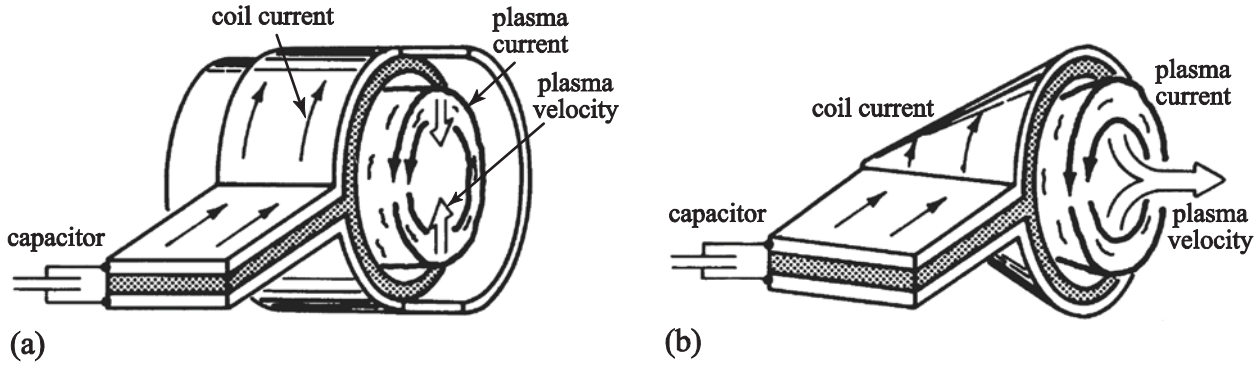

Figure 2

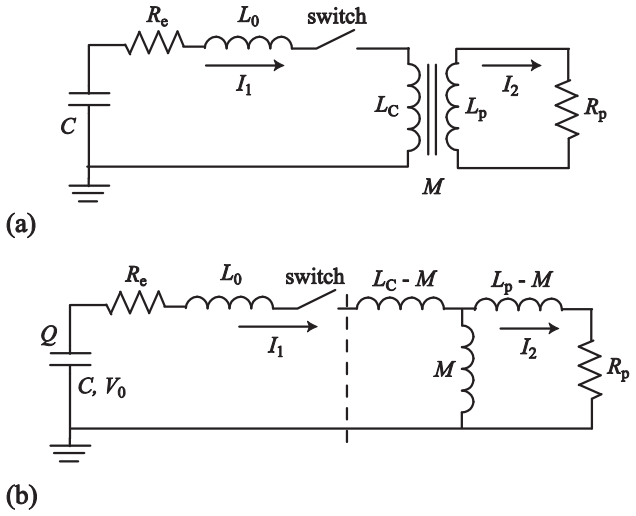

Figure 3

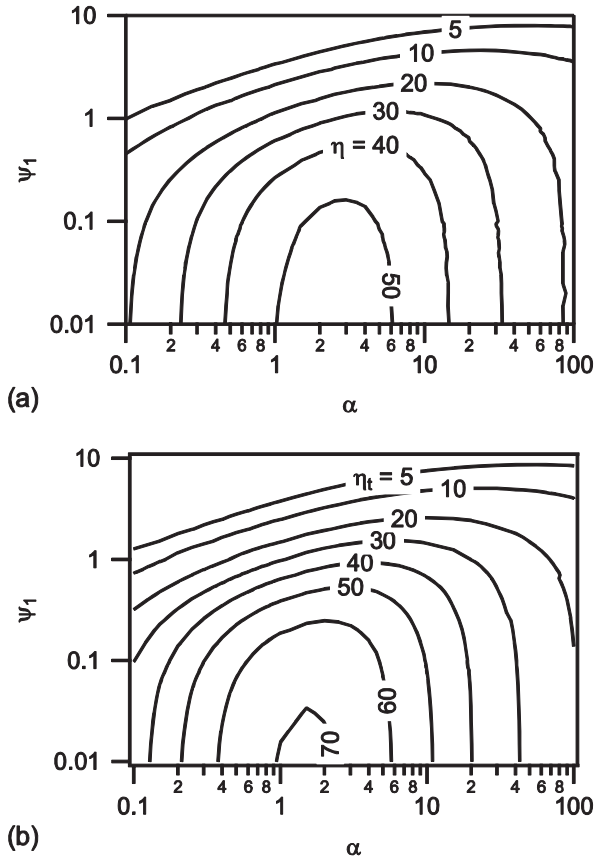

Figure 4

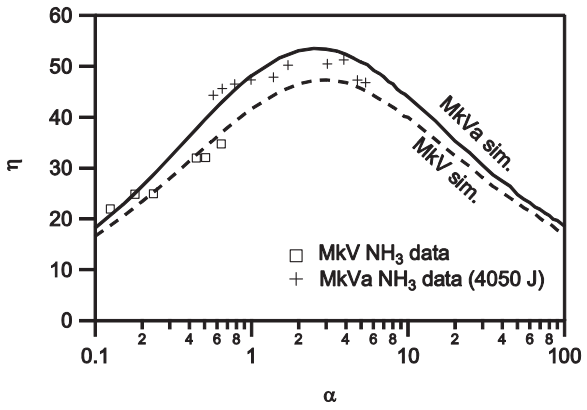

Figure 5

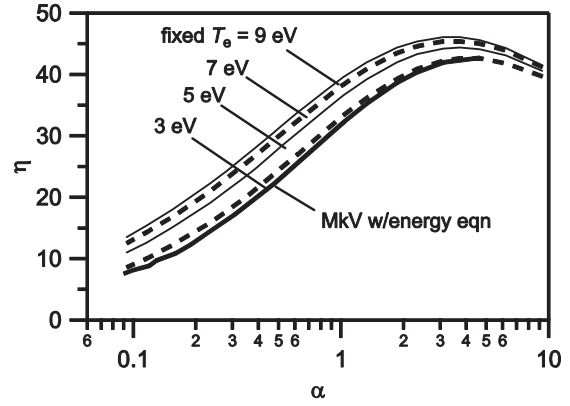

Figure 6